

Fast numerical method to generate halo catalogues in modified gravity (part I): second-order Lagrangian perturbation theory

C. Moretti ^{1,2,3}★, S. Mozzon, ^{1,4} P. Monaco, ^{1,2,3,5} E. Munari ² and M. Baldi ^{6,7,8}

¹Dipartimento di Fisica dell'Università di Trieste, Sezione di Astronomia, via Tiepolo 11, I-34143 Trieste, Italy

²INAF – Osservatorio Astronomico di Trieste, Via Tiepolo 11, I-34143 Trieste, Italy

³IFPU – Institute for Fundamental Physics of the Universe, Via Beirut 2, I-34014 Trieste, Italy

⁴Institute of Cosmology and Gravitation, University of Portsmouth, Burnaby Road, Portsmouth, PO1 3F, Burnaby Road, Portsmouth, UK

⁵INFN – Sezione di Trieste, Via Valerio 2, I-34127, Trieste, Italy

⁶Dipartimento di Fisica e Astronomia, Alma Mater Studiorum Università di Bologna, via Piero Gobetti, 93/2, I-40129 Bologna, Italy

⁷INAF – Osservatorio di Astrofisica e Scienza dello Spazio, via Piero Gobetti 93/3 1, I-40129 Bologna, Italy

⁸INFN – Sezione di Bologna, viale Berti Pichat 6/2, I-40127 Bologna, Italy

Accepted 2020 January 29. Received 2020 January 27; in original form 2019 September 11

ABSTRACT

We present a new numerical method to determine second-order Lagrangian displacement fields in presence of modified gravity (MG). We start from the extension of Lagrangian perturbation theory (LPT) to a class of MG models, which can be described by a parametrized Poisson equation. We exploit Fast Fourier transforms to compute the full source term of the differential equation for the second-order Lagrangian displacement field. We compare its mean to the source term computed for specific configurations, for which a k -dependent solution can be found numerically. We choose the configuration that best matches the full source term, thus obtaining an approximate factorization of the second-order displacement field as the space term valid for Λ Cold Dark Matter (Λ CDM) times a k -dependent, second-order growth factor. Such approximation is used to compute second-order displacements for particles. The method is tested against N -body simulations run with standard and $f(R)$ gravity: we rely on the results of a friends-of-friends code run on the N -body snapshots to assign particles to haloes, then compute the halo power spectrum. We find very consistent results for the two gravity theories: second-order LPT (2LPT) allows to recover the N -body halo power spectrum within ~ 10 per cent precision to $k \sim 0.2\text{--}0.4 h \text{Mpc}^{-1}$, as well as halo positions. We show that the performance of 2LPT with MG is the same (within 1 per cent) as the one obtained for standard Λ CDM case. This formulation of 2LPT can quickly generate dark matter distributions with $f(R)$ gravity, and can easily be extended to other MG theories.

Key words: methods: numerical – dark energy – large-scale structure of Universe – cosmology: theory.

1 INTRODUCTION

Ever since the discovery of the accelerated expansion of the Universe (Riess et al. 1998; Perlmutter et al. 1999), significant effort has been devoted to trying to explain the mechanism behind it. Even though the standard Λ cold dark matter (Λ CDM) cosmological model successfully fits most observations on large scales, the nature of dark energy is still one of the most challenging and elusive open questions in cosmology and fundamental physics. Shedding light on this topic is indeed a key target for future large-scale structure surveys, such as *Euclid* ¹ (Laureijs et al. 2011), DESI ² (Levi et al.

2013), LSST ³ (LSST Science Collaboration 2009), or *WFIRST* ⁴ (Spergel et al. 2013).

The Λ CDM model relies on the assumption that the growth of structures in the Universe is driven by gravitational instability, described by Einstein's general relativity (hereafter GR). Under this hypothesis, the simplest interpretation for the gravitationally repulsive fluid responsible for the cosmic accelerated expansion, and the only one that does not add new degrees of freedom, is that of a cosmological constant Λ . Its natural interpretation as the effect of vacuum energy poses strong theoretical problems, such as fine-tuning: the value of Λ needed to explain the recent accelerated expansion phase must be extremely small. This is in contrast to

* E-mail: chiara.moretti1989@gmail.com

¹<https://www.euclid-ec.org/>

²<https://www.desi.lbl.gov/>

³<https://www.lsst.org/>

⁴<https://wfirst.gsfc.nasa.gov/>

the value predicted by quantum field theory, which is orders of magnitude larger. The cosmological constant problems have been extensively discussed, see for example Weinberg (1989), Martin (2012).

An alternative to the introduction of a cosmological constant to explain the accelerated expansion is that GR is not the correct theory for gravity on cosmological scales. Precision cosmology, which holds the promise of providing accurate enough measurements to properly test different scenarios, has prompted the development of a large number of modified gravity models (hereafter MG, see for example Joyce et al. 2015; Bull et al. 2016; Amendola et al. 2018; Ishak 2019 for recent reviews on MG and cosmology). Admittedly, GR has successfully passed all tests up to now, from laboratory, to Solar system, to the recent breakthroughs provided by the observation of gravitational waves (Abbott et al. 2016) and the imaging of the black hole in M87 (Event Horizon Telescope Collaboration 2019). As a consequence, any alternative theory, in order to be viable, must satisfy very tight constraints. The proposed alternative models involve the introduction of an additional fifth force which adds to standard Newtonian gravity. The behaviour of the fifth force can be subdivided in three different regimes: on the largest scales it must mimic Λ CDM, but with a large deviation from GR, in order to explain the accelerated expansion without the need of a cosmological constant. On the smallest scales, the theory must reduce to GR: to achieve this, a screening mechanism must be introduced. Finally, there could still be deviations from GR on intermediate scales, where cosmological observables carry specific signatures that can help disentangling between different gravity theories.

Since possible signatures can be found in the mildly non-linear regime of structure formation, it is of crucial importance that accurate theoretical predictions are available, in order to compare to observations and place constraints on different models. The standard, and most reliable tools employed to achieve this goal are N -body simulations. However, full N -body simulations are computationally expensive, and even more so if they are run with MG. Their use becomes impractical, even in the standard GR case, when addressing the computation of covariance matrices of observables like the galaxy power spectrum or two-point correlation function; in this case, thousands of realizations are required to properly populate the matrices and suppress the sampling noise. For this reason, a variety of approximated numerical methods have been developed, such as those implemented in PINOCCHIO (PINpointing Orbit Crossing Collapsed Hierarchical Objects, Monaco, Theuns & Taffoni 2002; Munari et al. 2017b), COLA (Tassev, Zaldarriaga & Eisenstein 2013; Izard, Crocce & Fosalba 2016; Koda et al. 2016), PEAK PATCH (Bond & Myers 1996; Stein, Alvarez & Bond 2019), PATCHY (Kitaura, Yepes & Prada 2014), and HALOGEN (Avila et al. 2015). For a recent review on approximated methods to generate halo catalogues, see Monaco (2016). These methods have been tested in the context of the standard Λ CDM scenario (see Blot et al. 2019; Colavincenzo et al. 2019; Lippich et al. 2019 for a comparison between different software). Many of these methods are based on Lagrangian perturbation theory (LPT), so extending them to MG theories requires to extend LPT first. This has been done by several authors, like Aviles & Cervantes-Cota (2017), and the extensions of the COLA approach to scalar-tensor MG theories presented by Valogiannis & Bean (2017) and Winther et al. (2017). Recently, the PINOCCHIO code has been extended to massive neutrino cosmologies (Rizzo et al. 2017). That extension was based on the numerical result of Castorina et al. (2014) that the halo mass function in presence of massive neutrinos can be obtained,

with good accuracy, by using the the dark matter (plus baryons) power spectrum, as if perturbations in the neutrino component were always linear. The free streaming of massive neutrinos imprints a scale dependence on the linear growth factor, $D_1 = D_1(k, t)$. This function was obtained from the growth of the linear power spectrum as predicted by the CAMB software (Lewis & Bridle 2002), while the second-order growth rate was obtained using the fit proposed by Bouchet et al. (1995), valid for GR in Λ CDM model: $D_2 = -3/7 D_1^2 \Omega_m^{-1/143}$. This approach was adequate in the case of massive neutrinos, where the scale-dependent growth is due to the relativistic component but gravity is standard GR. As we will show later, in Section 5, this simple technique does not give accurate results when dealing with modifications of the gravity theory.

In this paper, we present and test a fast numerical method to compute 2LPT displacements with a class of MG scalar-tensor theories, specializing it to the case of $f(R)$ gravity. This is the first step towards a full extension of the PINOCCHIO code. The main problem to face is the fact that, unlike in the case of standard GR, the LPT displacement terms cannot be factorized into space- and time-dependent functions. At second order this leads to a very complicated integro-differential equation, whose numerical solution is very hard to obtain. Winther et al. (2017) already proposed an approximate way to achieve a factorization into a space-dependent part and a mildly scale-dependent growth factor $D_2(k, t)$. With respect to that work, we quantify the error made by approximating the full source term of the equation of the 2LPT displacement potential, and investigate the effect of this error by predicting the non-linear power spectrum of dark matter haloes and comparing to the one measured from the output of an N -body simulation run with MG-GADGET (Puchwein, Baldi & Springel 2013) with $f(R)$ gravity.

The paper is structured as follows: in Section 2.1, we give an overview of LPT for the standard Λ CDM model. In Section 2.2, we summarize the equations used to extend LPT to scalar-tensor theories, and introduce the $f(R)$ MG model we are considering. In Section 3, we describe a new numerical method that allows to compute the full source term of the second-order differential equation for the displacement field. This allows to test different configurations in order to find the one that best matches the full solution, as well as to quantify the error introduced by approximating the second-order growth factor. We perform a specific test by comparing to the outputs of a full N -body simulation, presented in Section 4, to validate our method. In Section 5, we also test the approximation proposed by Bouchet et al. (1995) to compute the second-order growth factor from $D_1(k, a)$, showing that this approach is not suitable in the case of MG. In Section 6, we draw our conclusions and discuss future works.

2 THEORETICAL FRAMEWORK

2.1 Lagrangian perturbation theory in Λ CDM

LPT, pioneered by Zel'dovich (Zel'dovich 1970, see Bouchet 1996 for a review), has proven a very powerful tool and is indeed the foundation on which many approximated methods rely. It is based on a Lagrangian description of the dynamics of cosmic fluids, following particles' trajectories instead of studying the evolution of the density and velocity fields in a fixed frame as in Eulerian perturbation theory. It can be seen as a coordinate change, with the main quantity being the displacement field Ψ which maps the initial position \boldsymbol{q} of a fluid element to the final, Eulerian position \boldsymbol{x}

through

$$\mathbf{x}(\mathbf{q}, a) = \mathbf{q} + \Psi(\mathbf{q}, a), \quad (1)$$

where a is the scale factor. As long as the displacement is small, it can be expanded in a perturbation series; moreover, as long as Ψ is curl free (since it is second-order), it can be written as the gradient of a scalar potential ϕ :

$$\Psi(\mathbf{q}, a) = \nabla_{\mathbf{q}} \phi(\mathbf{q}, a), \quad (2)$$

with $\nabla_{\mathbf{q}} = \partial/\partial\mathbf{q}$ being the gradient in Lagrangian coordinates. The equation of motion for the particle trajectory can be written as

$$a^2 H^2(a) \left[\frac{d^2}{da^2} + \left(\frac{3}{a} + \frac{H'(a)}{H(a)} \frac{d}{da} \right) \right] \mathbf{x} = a^2 H^2 \hat{T} \mathbf{x} = -\nabla_{\mathbf{x}} \Phi_N, \quad (3)$$

where the $'$ denotes derivation with respect to the scale factor, $H(a)$ is the Hubble parameter, Φ_N is the gravitational potential and we defined the \hat{T} operator as the quantity between square brackets in equation (3). Note that here $\nabla_{\mathbf{x}} = \partial/\partial\mathbf{x}$ is the gradient in Eulerian coordinates. By imposing matter conservation, it is possible to write the relation between the displacement field and the overdensity δ :

$$\delta(\mathbf{x}, a) = \frac{1 - J(\mathbf{q}, a)}{J(\mathbf{q}, a)}, \quad (4)$$

where $J(\mathbf{q}, a)$ is the determinant of the Jacobian of the transformation:

$$J_{ij} = \frac{\partial x^i}{\partial q^j} = \delta_{ij} + \frac{\partial \Psi^i}{\partial q^j}. \quad (5)$$

By taking the divergence of equation (3) together with the Poisson equation and equation (4), we can write the evolution equations for the first- and second-order Lagrangian potentials:

$$\begin{aligned} a^2 H^2 (\hat{T} - 4\pi G \bar{\rho}) \phi_{,ii}^{(1)} &= 0, \\ a^2 H^2 (\hat{T} - 4\pi G \bar{\rho}) \phi_{,ii}^{(2)} &= -4\pi G \bar{\rho} \left[\frac{1}{2} (\phi_{,ii} \phi_{,jj} - \phi_{,ij} \phi_{,ji}) \right]. \end{aligned} \quad (6)$$

Here, i denotes the derivative with respect to q_i , and we adopt the standard notation of summation over repeated indices. Since the operator acting on $\phi^{(1)}$ and $\phi^{(2)}$ is only a function of time, the time evolution can be factored out and the potentials can be written as the (time-dependent) growth factors times the initial potentials:

$$\begin{aligned} \phi^{(1)}(\mathbf{q}, a) &= D_1(a) \phi^{(1)}(\mathbf{q}, a_{in}), \\ \phi^{(2)}(\mathbf{q}, a) &= D_2(a) \phi^{(2)}(\mathbf{q}, a_{in}). \end{aligned} \quad (7)$$

Given an initial displacement field, the computation of potentials and displacements for any time is thus straightforward, once the equation for the first- and second-order growth factors are solved:

$$\begin{aligned} a^2 H^2 (\hat{T} - 4\pi G \bar{\rho}) D_1(a) &= 0, \\ a^2 H^2 (\hat{T} - 4\pi G \bar{\rho}) D_2(a) &= -4\pi G \bar{\rho} D_1^2(a), \end{aligned} \quad (8)$$

The initial, first-order potential is directly linked to the density field through equation (4):

$$\phi_{,ii}^{(1)}(\mathbf{q}, a_{in}) = -\delta^{(1)}(\mathbf{q}, a_{in}), \quad (9)$$

while the second-order can be written as

$$\phi_{,ii}^{(2)}(\mathbf{q}, a_{in}) = \frac{1}{2} \left[\phi_{,ii}^{(1)} \phi_{,jj}^{(1)} - \phi_{,ij}^{(1)} \phi_{,ji}^{(1)} \right](\mathbf{q}, a_{in}), \quad (10)$$

and can be easily and readily computed with Fast Fourier transforms (FFTs) from the initial first-order Lagrangian potential $\phi^{(1)}(\mathbf{q}, a_{in})$.

The possibility to factor out the time evolution to compute displacements in the particles' positions is the key feature that makes this approach ideal to be implemented in fast, approximated methods that simulate the formation of the large-scale structure of the Universe. However, as anticipated above and described in detail in Section 2.4, one effect of MG is that the growth factors become scale dependent. As a consequence, separating out the time evolution to compute displacements at any given time is not possible anymore, and both the theoretical and computational treatment of LPT with MG become more involved.

2.2 Modified gravity

In this work, we focus on MG models that mimic Λ CDM on large scales, while on intermediate scales they include a fifth force that is due to a new scalar degree of freedom. Moreover, they need a screening mechanism to comply with tight Solar system constraints at small scales. The fifth force caused by the gravity modification introduces mode coupling even at the linear level; additionally, in order to properly describe non-linear scales, the Klein–Gordon equation for the scalar field must be solved. Following the approach of Koyama, Taruya & Hiramatsu (2009), the modified Poisson equation and the Klein–Gordon equation can be written as

$$\frac{1}{a^2} \nabla^2 \Phi = 4\pi G \bar{\rho} \delta - \frac{1}{2a^2} \nabla^2 \varphi, \quad (11)$$

$$(3 + 2\omega_{\text{BD}}) \frac{1}{a^2} \nabla^2 \varphi = -8\pi G \bar{\rho} \delta + \text{NL}, \quad (12)$$

where Φ is the gravitational potential, $\bar{\rho}$ is the background matter density, φ is the scalar field that encodes the modification of gravity, ω_{BD} is the Brans–Dicke parameter, and NL are possible non-linearities that might arise in the Lagrangian. Going to Fourier space, equation (12) can be written as

$$(3 + \omega_{\text{BD}}) \frac{k^2}{a^2} \varphi_k = 8\pi G \bar{\rho} \delta_k - \mathcal{I}(\varphi_k). \quad (13)$$

The term $\mathcal{I}(\varphi_k)$ is the scalar field self-interaction, which is related to the screening mechanism responsible of recovering GR on small scales. It can be expanded as $\mathcal{I}(\varphi_k) = M_1(k, a) \varphi_k + \delta \mathcal{I}(\varphi_k)$, with

$$\begin{aligned} \delta \mathcal{I}(\varphi_k) &= \frac{1}{2} \int \frac{d^3 k_1 d^3 k_2}{(2\pi)^3} \delta_D(\mathbf{k} - \mathbf{k}_{12}) M_2(\mathbf{k}_1, \mathbf{k}_2, a) \\ &\quad \times \varphi(\mathbf{k}_1, a) \varphi(\mathbf{k}_2, a) + \mathcal{O}(\varphi_k^3), \end{aligned} \quad (14)$$

where the M_i functions are in general scale and time dependent and their functional form depends on the particular model considered. In the following section, we will focus on scalar–tensor theories of gravity, targeting in particular the $f(R)$ family of gravity models (see De Felice & Tsujikawa 2010 for a review). Our method however is general, and can be applied to other scalar–tensor theories, provided that the MG potential can be split in a background value plus perturbations, and the perturbations can be Taylor expanded (see equation 18 below).

2.3 $f(R)$ gravity

In $f(R)$ models, the Einstein–Hilbert Lagrangian density is modified to include a function of the Ricci scalar R :

$$\mathcal{L}_R = \sqrt{-g} (R + f(R)). \quad (15)$$

This possible extension to GR has been widely developed, both in terms of theoretical predictions and possible observational signatures. The functional form of $f(R)$ is bounded by the requirement of

satisfying Solar system constraints and reproducing the Λ CDM expansion history; several functional forms meet these requirements. The one we are considering in this paper is that described in Hu & Sawicki (2007). While constraints on model parameters are getting tighter and tighter, particular effort has recently been put into investigating them in light of the degeneracy with the mass of neutrinos (see e.g. Baldi et al. 2014; Hu et al. 2015; Giocoli, Baldi & Moscardini 2018; Wright et al. 2019).

By varying the action constructed with the modified Lagrangian of equation (15) with respect to the metric, and then taking the trace of the resulting field equations, one obtains:

$$3\Box f_R = R(1 - f_R) + 2f - 8\pi G\rho, \quad (16)$$

where $f_R = df(R)/dR$. Equivalently, one can split f_R and R in background quantities plus perturbations δf_R and δR . In the quasi-static approximation one can write:

$$\frac{3}{a^2}\nabla^2\delta f_R = -8\pi G\bar{\rho}\delta + \delta R, \quad (17)$$

which is nothing but the Klein–Gordon equation for a scalar field with potential δR and Brans–Dicke parameter $\omega_{\text{BD}} = 0$. The potential can be expanded as

$$\delta R = \sum_k \frac{1}{k!} M_k (\delta f_R)^k, \quad M_k = \left. \frac{d^k R(f_R)}{d f_R^k} \right|_{f_R = \bar{f}_R} \quad (18)$$

For $f(R)$ gravity, the coefficients M_k only depend on time; this is an important feature to the approach we propose in this work (described in Section 3). In the following treatment, we will consider Hu–Sawicki $f(R)$, for which we have:

$$f(R) = -\beta^2 \frac{c_1(R/\beta^2)^n}{c_2(R/\beta^2)^n + 1}, \quad (19)$$

where β^2 is the mass scale, defined as $\beta^2 = H_0^2 \Omega_{\text{m},0}$, and c_1, c_2 , and n are free parameters of the model. The model is consistent with a Λ CDM background expansion if one chooses $c_1/c_2 = 6\Omega_\Lambda/\Omega_{\text{m},0}$, thus leaving only two free parameters that can be recast in terms of the value of f_R today, f_{R0} , and n . By fixing $n = 1$, the M_k coefficients can be written as

$$M_1(a) = \frac{3}{2} \frac{H_0^2}{|f_{R0}|} \frac{(\Omega_{\text{m},0} a^{-3} + 4\Omega_\Lambda)^3}{(\Omega_{\text{m},0} + 4\Omega_\Lambda)^2},$$

$$M_2(a) = \frac{9}{4} \frac{H_0^2}{|f_{R0}|^2} \frac{(\Omega_{\text{m},0} a^{-3} + 4\Omega_\Lambda)^5}{(\Omega_{\text{m},0} + 4\Omega_\Lambda)^4}. \quad (20)$$

2.4 LPT with modified gravity

A proper formulation of LPT in the framework of scalar–tensor MG theories has been proposed only recently (see Aviles & Cervantes-Cota 2017; Valogiannis & Bean 2017; Winther et al. 2017). For a full theoretical description we refer to Aviles & Cervantes-Cota (2017), where a general formalism to compute Lagrangian displacement fields with MG up to third order was presented; here, we report just the basic equations necessary to describe our method.

By substituting equation (13) in the Fourier space version of the modified Poisson equation (11), and then combining with the equation of motion (3), we can write the evolution equation for the first-order displacement field in Fourier space as

$$a^2 H^2 (\hat{T} - 4\pi G \bar{\rho} \mu(k, a)) \text{FT} \left[\phi_{,ii}^{(1)} \right] (\mathbf{k}, a) = 0, \quad (21)$$

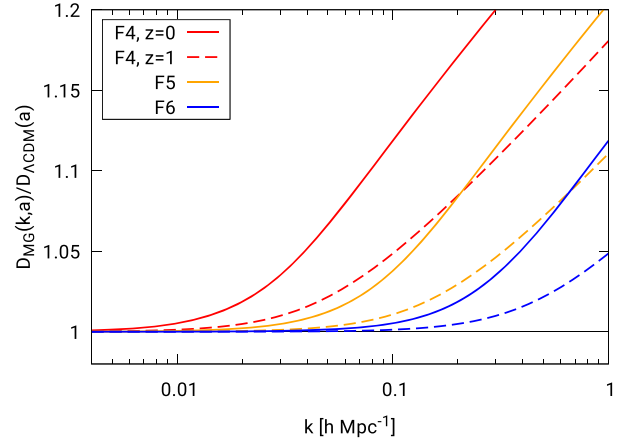


Figure 1. Solution to equation (24) for Hu–Sawicki $f(R)$ with $n = 1$ normalized to the Λ CDM linear growing mode for three different values of the f_{R0} parameter ($f_{R0} = -10^{-4}$ in red, labelled as F4; $f_{R0} = -10^{-5}$ in orange, labelled as F5; $f_{R0} = -10^{-6}$ in blue, labelled as F6), shown for $z = 0$ (solid line) and $z = 1$ (dashed line).

where FT is the Fourier transform operator, and

$$\mu(k, a) = 1 + \frac{1}{3} \frac{k^2/a^2}{k^2/a^2 + m^2(a)}. \quad (22)$$

The $m^2(a)$ function represents the mass of the scalar field, and is related to $M_1(a)$ by $M_1(a) = 3m^2(a)$. It is no longer possible to separate time and space, since the operator acting on the first-order displacement potential is no longer time-dependent only, due to the presence of $\mu(k, a)$ in equation (21). None the less, we can separate time for each Fourier mode, so that

$$\text{FT} \left[\phi_{,ii}^{(1)} \right] (\mathbf{k}, a) = D_1(k, a) \text{FT} \left[\phi_{,ii}^{(1)} \right] (\mathbf{k}, a_{\text{in}}), \quad (23)$$

where $D_1(k, a)$ is the solution of

$$a^2 H^2 (\hat{T} - 4\pi G \bar{\rho} \mu(k, a)) D_1(k, a) = 0. \quad (24)$$

We note that the first-order growth factor is now scale dependent, due to the presence of the $\mu(k, a)$ function in the differential equation. However, the scale dependence is fully enclosed in μ , and is only related to the modulus of k . The linear growth factor can then be computed by fixing a value for k and solving the differential equation, then repeating for a set of k -values and finally interpolating to obtain the function at any k . We numerically solve equation (24) with a standard Runge–Kutta algorithm, with initial conditions for $D_1(k, a)$ set to the growing mode for a matter-dominated (Einstein–de Sitter) universe, namely $D_1(a_{\text{in}}) = a_{\text{in}}$ and $D_1'(a)|_{a=a_{\text{in}}} = 1$. The resulting linear growth factor is then normalized so that $D_1(k = 0, a = 1) = 1$. The result is shown in Fig. 1, where we plot the ratio between the MG linear growth factor D_{MG} and the Λ CDM one in the case of $n = 1$ Hu–Sawicki $f(R)$, for three different values of the f_{R0} parameter and two different redshifts. Once again, the initial first-order displacement field can be determined from the initial density field, and its evolution computed by multiplying it by $D_1(k, a)$. However, when going to second order this kind of separation cannot be done; the second-order growth factor now depends on three wave-numbers k, k_1 , and k_2 and on the dot product $\mathbf{k}_1 \cdot \mathbf{k}_2$. The second-order displacement field can be written (in Fourier space) as an integral over k_1 and k_2 :

$$\text{FT} \left[\phi_{,ii}^{(2)} \right] (\mathbf{k}, a) = \int \frac{d^3 k_1 d^3 k_2}{(2\pi)^3} \delta_D(\mathbf{k} - \mathbf{k}_{12}) D_2(k, k_1, k_2, a) \delta_1 \delta_2, \quad (25)$$

where δ_D is the Dirac's delta, $\mathbf{k}_{12} = \mathbf{k}_1 + \mathbf{k}_2$, $\delta_i = \delta(\mathbf{k}_i)$ is the linear density contrast evaluated at present time, and $D_2(k, k_1, k_2, a)$ is the scale-dependent second-order growth rate obtained by solving (see Aviles & Cervantes-Cota 2017, where a full derivation of the following equation can be found)

$$\begin{aligned}
 & a^2 H^2(a) [\hat{T} - 4\pi G \bar{\rho} \mu(k)] D_2(k, k_1, k_2, a) \\
 &= 4\pi G \bar{\rho} D_1(k_1, a) D_1(k_2, a) \left\{ \mu(k) \right. \\
 &\quad - \frac{(\mathbf{k}_1 \cdot \mathbf{k}_2)^2}{k_1^2 k_2^2} [\mu(k_1) + \mu(k_2) - \mu(k)] \\
 &\quad + \frac{m^2(a)}{\Pi(k)} \left[2 \frac{(\mathbf{k}_1 \cdot \mathbf{k}_2)^2}{k_1^2 k_2^2} (\mu(k_1) + \mu(k_2) - 2) \right. \\
 &\quad \left. + \frac{\mathbf{k}_1 \cdot \mathbf{k}_2}{k_1^2} (\mu(k_1) - 1) + \frac{\mathbf{k}_1 \cdot \mathbf{k}_2}{k_2^2} (\mu(k_2) - 1) \right] \\
 &\quad \left. - \frac{2}{27} 4\pi G \bar{\rho} \frac{k^2}{a^2} \frac{M_2(a)}{\Pi(k)\Pi(k_1)\Pi(k_2)} \right\}. \quad (26)
 \end{aligned}$$

Here, we did not explicitly write the time dependence of $\mu(k, a)$ and $\Pi(k, a)$ in the previous equation to simplify it.

The presence of the Dirac's delta in equation (25) requires that $\mathbf{k} = \mathbf{k}_1 + \mathbf{k}_2$, so that the integral runs over all possible triangle configurations formed by \mathbf{k}_1 , \mathbf{k}_2 , and \mathbf{k} in Fourier space. Because of this, implementing the full solution for the second-order displacements would require to solve a different equation for each wavenumber \mathbf{k} , whose source term includes a nine-dimensional integral. While not unfeasible in principle, this computation would be very time consuming, making 2LPT a poor alternative to full N -body simulations.

One possible alternative, already explored by Winther et al. (2017), is to find an approximation for $D_2(k, a)$, in order to achieve an effective factorization of the second-order potential into the same space part as in GR (to be computed with FFTs) and an effective k -dependent growth rate

$$\phi^{(2)}(\mathbf{k}, a) = D_2(k, a) \phi^{(2)}(\mathbf{k}, a_{in}). \quad (27)$$

In particular, one can choose a triangle configuration for \mathbf{k} , \mathbf{k}_1 , and \mathbf{k}_2 , solve equation (26) to find $D_2(k, k_1, k_2, a)$, and then compute the displacement field in the standard way, with $\phi^{(2)}(\mathbf{k}, a_{in})$ being the Fourier space version of the initial second-order displacement field of equation (10).

3 METHOD: APPROXIMATING THE 2LPT DISPLACEMENT FIELD

As discussed in the previous section, our goal is to find an approximation for the second-order growth rate which allows to readily compute the second-order displacement field. Moreover, we want to quantify the deviation of the approximation from the full solution. Our approach is to compute the full source term of the differential equation for the 2LPT displacement field by taking advantage of FFTs, and then compare it to analytical expressions for different triangle configurations, in order to find the one that best matches the full source term. Next, we numerically solve the differential equation for D_2 for the chosen triangle configuration, and use it to approximate the evolution of the displacement field.

The second-order displacement field in general, scalar–tensor theories of gravity (where the scalar field potential can be expanded

as in equation 18) is the solution of equation (25). The growth factor can be computed by solving equation (26). This equation reduces to the standard, Λ CDM one for $\mu(k, a) = 1$. The dependence on closed triangles in Fourier space is related to the presence of derivatives of the first-order displacement field as well as the M_k functions, which can in principle bear a scale dependence. In the special case of $f(R)$ gravity theories, the M_k functions only depend on time, so they can be taken out of the integral we need to solve to compute $\phi^{(2)}(\mathbf{k}, a)$. Equation (25) can then be written by expressing the Fourier space integrals as Fourier transforms of local, non-linear functions in real space. It is then possible to take advantage of FFTs to compute the full source term of the differential equation. The validity of this approach is not limited to $f(R)$ models but extends to all theories where the MG scalar potential can be expanded into scale-independent coefficients. The full equation for 2LPT displacements can be written as

$$a^2 H^2 (\hat{T} - 4\pi G \bar{\rho} \mu(k, a)) \text{FT} \left[\phi_{,ii}^{(2)} \right] (\mathbf{k}, a) = S_1 + S_2 + S_3 + S_4, \quad (28)$$

where

$$S_1 = 4\pi G \bar{\rho} \text{FT} \left[\phi_{,ij}^{(1)} \text{FT}^{-1} \left[\mu(k, a) \text{FT} \left[\phi_{,ji}^{(1)} \right] \right] \right], \quad (29)$$

$$S_2 = -2\pi G \bar{\rho} \mu(k, a) \text{FT} \left[\phi_{,ii}^{(1)} \phi_{,jj}^{(1)} - \phi_{,ij}^{(1)} \phi_{,ji}^{(1)} \right], \quad (30)$$

$$S_3 = \left(\frac{8\pi G \bar{\rho}}{3} \right)^2 \frac{M_2(a)}{12} \frac{k^2/a^2}{\Pi(k, a)} \text{FT} \left[\left(\text{FT}^{-1} \left[\frac{\delta_k^{(1)}}{\Pi(k, a)} \right] \right)^2 \right], \quad (31)$$

$$\begin{aligned}
 S_4 = & -\frac{8\pi G \bar{\rho}}{3} \frac{m^2(a)}{2a^2} \frac{1}{\Pi(k, a)} \text{FT} \left[2\phi_{,ij}^{(1)} \left(\text{FT}^{-1} \left[\frac{\delta_k^{(1)}}{\Pi(k, a)} \right] \right) \right]_{,ij} \\
 & + \phi_{,ij}^{(1)} \left(\text{FT}^{-1} \left[\frac{\delta_k^{(1)}}{\Pi(k, a)} \right] \right)_{,j}. \quad (32)
 \end{aligned}$$

Here, $\Pi(k, a) = k^2/a^2 + m^2(a)$ and the $\phi^{(1)}$, $\delta^{(1)}$ fields are evolved with the linear scale-dependent growth factor $D_1(k, a)$. The S_1 and S_2 terms come from keeping second-order terms in the Poisson equation and the equation of motion. The S_3 term is related to the second-order scalar field self-interaction (NL in equation 12). Finally, the S_4 term (first introduced by Aviles & Cervantes-Cota 2017), is a geometric term, due to the fact that we are performing Fourier transforms in Lagrangian Fourier space, not Eulerian.

The method we adopt is the following: we generate a linear density field on a regular grid; we compute the first-order growth factor $D_1(k, a)$ by numerically solving equation (24), then use it to evolve the field. Next, we compute the S_i terms of equation (28), going back and forth from Fourier space to configuration space to solve the integrals. We divide the source term by the equivalent quantity evaluated for Λ CDM. The result is a quantity that depends on \mathbf{k} , which we bin in a grid of k -values, computing its average and scatter within each bin. Then, we compare this average with the analytical expressions obtained using various triangle configurations in Fourier space. The result is shown in Fig. 2, where we show the computation of the full source term of the differential equation divided by its equivalent evaluated for a Λ CDM cosmology, at $z = 0$. The solid lines represent the source term for boxes with different sizes (200, 400, 600, and 700 Mpc h^{-1}) with a fixed resolution of 1 particle/Mpc h^{-1} . For each box, we produce two realizations, one

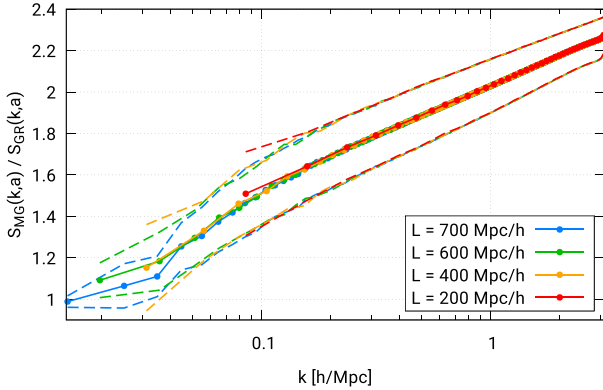


Figure 2. Source term of the second-order displacement field differential equation with $f(R)$ MG, normalized to the one in GR at $z = 0$. The MG model is $n = 1$ Hu–Sawicki with $f_{R0} = -10^{-4}$. The different colours correspond to different box sizes, all with the same resolution of 1 particle per $\text{Mpc } h^{-1}$. Each solid line is the result binned in k ; the dashed lines represent 1σ deviation from the mean value within each k -bin.

with MG and one with standard GR, both with the same initial conditions in order to have the same modes and sample variance. We then compute the ratio of the two and compute average and standard deviation in bins of k . The dashed lines show the obtained 1σ standard deviation of the distribution of the points in each bin: this represents the scatter, due to the fact that the source term depends on the vector \mathbf{k} . This scatter provides a measure of how accurate a factorization in terms of a mildly k -dependent growth rate $D_2(k, t)$ is: even though the source term is not completely separable, the standard deviation is always below ~ 0.2 , and goes to zero at large scales, as expected. Moreover, the average varies smoothly with k , and the standard deviation of the mean within each bin is not large, $\sigma/\sqrt{N} \sim 10^{-6}$ (with N the number of wave-modes in each bin). We can conclude that the average is measured with a good precision, and can be used to the purpose of finding an approximation to D_2 . We then compare the average ratio of source term to the same quantity, obtained analytically by adopting different triangle configurations: the result is shown in Fig. 3. The top panel shows the full source term (divided by the GR one) of Fig. 2 with black dots, and different triangle configurations (solid lines), while in the bottom panel we show the percent difference between the full source term and different triangle configurations. First, we compare to orthogonal ($k_1 = k_2, \theta = 90^\circ$), equilateral ($k_1 = k_2, \theta = 60^\circ$), and squeezed ($k_1 \simeq 0, k_2 = k$) configurations. We find the solution to be very close to the orthogonal configuration, and above the equilateral one. These are both isosceles triangles with $k_1 = k_2$ and angle between \mathbf{k}_1 and \mathbf{k}_2 , respectively, $\theta = 90^\circ$ and $\theta = 60^\circ$. We therefore focus on isosceles triangles, keeping $k_1 = k_2$ and varying the angle. We find the best configuration to be the orthogonal one (red line in Fig. 3, hereafter T1) and the one with $\theta = 80^\circ$ (orange line in Fig. 3, hereafter T2). We find that both T1 and T2 give results that are well within 1 per cent with respect to the full source term, in particular for the mildly intermediate scales we are interested in describing with 2LPT. We also compare the source term to triangle configurations with different ratio k_1/k_2 and fixed angle 80° , finding that increasing the ratio k_1/k_2 gives a worse match to the source term (green and magenta lines of Fig. 3). The approximation proposed by Winther et al. (2017) is shown in blue in Fig. 3, and corresponds to fixing $k_1 = k_2, \theta = 90^\circ$ in equation (26), but the first-order growth rates in that equation are computed as $D_1(k)$ instead of $D_1(k_1), D_1(k_2)$. This choice gives a

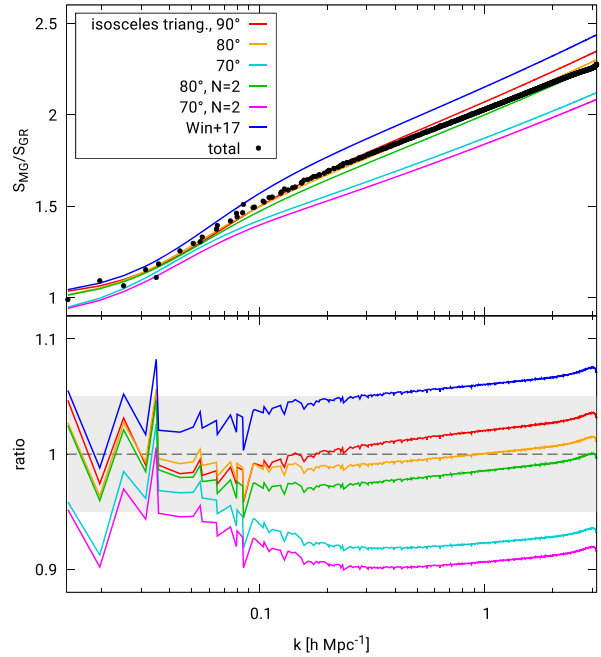


Figure 3. Top panel: comparison of the full source term (black dots) to different triangle configurations at redshift $z = 0$. The red, orange, and cyan lines represent isosceles triangles, respectively, with angle 90° (orthogonal configuration), 80° , and 70° between k_1 and k_2 . The green and magenta lines represent triangles with $k_1 = 2k_2$ and angle 80° and 70° , respectively, between k_1 and k_2 . In blue is shown the approximation adopted in Winther et al. (2017). Bottom panel: ratio of the full solution to different configurations. The grey shaded area represents a 5 per cent deviation from the full source term.

slight overestimation of the source term, but the deviation is still within 5 per cent up to $k \sim 0.2h \text{ Mpc}^{-1}$.

To understand the generality of this result, we perform the same computation for three different redshifts ($z = 0, z = 0.5$, and $z = 1$) and three different values of the f_{R0} parameter ($f_{R0} = -10^{-4}$, F4; $f_{R0} = -10^{-5}$, F5; $f_{R0} = -10^{-6}$, F6). The result is shown in Fig. 4. The black dots represent the result of the ratio of source terms S_{MG}/S_{GR} , while the solid lines represent the two best triangles found for the F4, $z = 0$ case: T1 in red and T2 in green. We note that, when considering different redshifts and values of f_{R0} , the T1 configuration approximates better the full source term, therefore we adopt it to compute the approximate $D_2(k, a)$ in the comparison to full N -body simulations.

4 TEST AGAINST N -BODY SIMULATIONS

To test how well our approximation for second-order displacements does at reconstructing the positions of dark matter haloes, we use a suite of N -body simulations run with $f(R)$ gravity (Giocoli et al. 2018), the DUSTGRAIN pathfinder simulations. These simulations are performed with the MG–GADGET code (Puchwein et al. 2013) and consist of 768^3 particles of mass $8.1 \times 10^{10} M_\odot$ in a $750 \text{ Mpc } h^{-1}$ side box. The adopted cosmology comes from Planck 2015 (Planck Collaboration 2016): $\Omega_m = 0.31345$, $\Omega_b = 0.0481$, $\Omega_\Lambda = 0.68655$, $H_0 = 67.31 \text{ km s}^{-1} \text{ Mpc}^{-1}$, $A_s = 2.199 \times 10^{-9}$, $n_s = 0.9658$. The MG model is Hu–Sawicki $f(R)$ with $n = 1$, and three different values of $f_{R0} = -10^{-4}$ (F4), -10^{-5} (F5), -10^{-6} (F6). For our tests, we use the simulation with $f_{R0} = -10^{-4}$ to maximize deviations from GR, and we compare the halo power spectrum we derive to the one

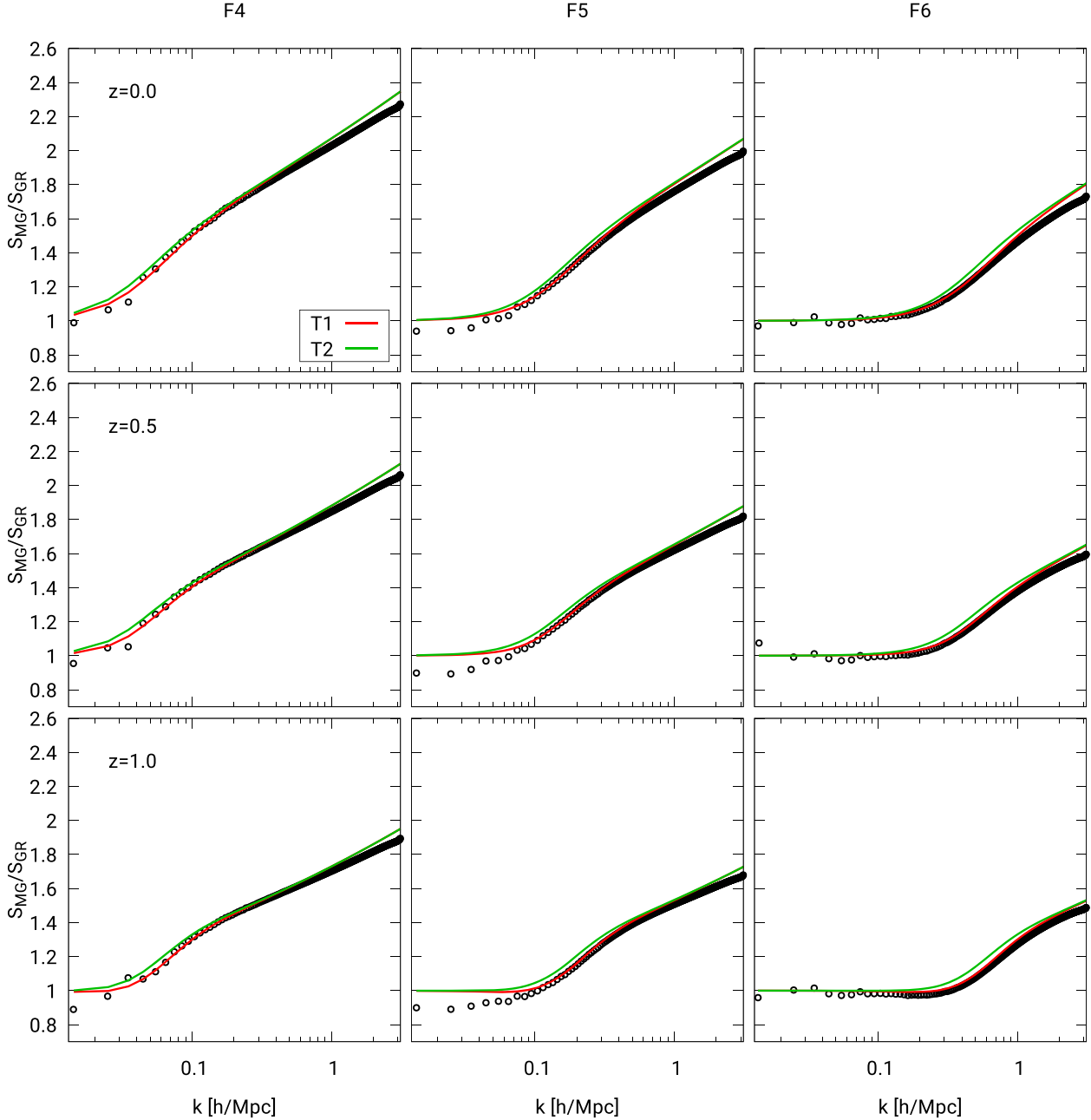


Figure 4. Computation of the full source term (black dots), compared to the triangle configurations T1 (orthogonal: $k_1 = k_2$, $\theta = 90^\circ$, red line) and T2 ($k_1 = k_2$, $\theta = 80^\circ$, green line), for different redshifts and different values of the f_{R0} parameter. Top row is $z = 0$, middle row $z = 0.5$, and bottom row is for $z = 1$. The left column is $f_{R0} = -10^{-4}$, middle column $f_{R0} = -10^{-5}$, and right column $f_{R0} = -10^{-6}$. For each redshift and each value of f_{R0} , we compute the source term for a box with 700^3 particles and $L = 700 \text{ Mpc } h^{-1}$.

measured in the simulations. A reference Λ CDM simulation is also available. Haloes are found by running a standard friends-of-friends halo finder on the simulation snapshots, using a linking length of 0.2 times the interparticle distance.

Our goal is to assess the performance of our approximation for 2LPT in the context of MG models. For this purpose, we conduct an analysis similar to the one carried out in Munari et al. (2017a): we set up our code using the same initial conditions of the N -body simulation, distributing particles on a regular grid. Particles in the same Lagrangian positions are labelled with the same IDs as in the N -body simulation. We displace particles using

our approximation for second-order LPT and group them in haloes using the same membership of the simulation. Finally, we construct the halo catalogue, computing the position of each halo by averaging over the particles that belong to it. From our reconstructed catalogue, we evaluate the halo power spectrum, using the method described in Sefusatti et al. (2016), both for our catalogue and the simulation's one. The result is shown in Fig. 5 for three different redshifts: $z = 0, 0.2, 1.0$. The MG model chosen is again Hu–Sawicki $f(R)$ with $n = 1$ and $f_{R0} = -10^{-4}$. Here, we plot the ratio of the halo power spectrum obtained when displacing particles with our approximation to the one measured from simulations. We show results for the Zel'dovich

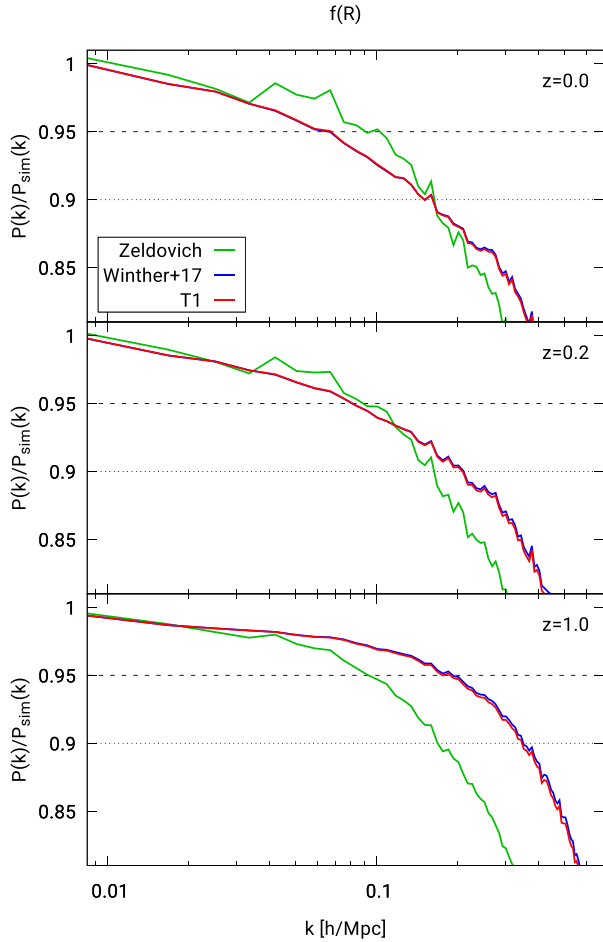


Figure 5. Ratio of the halo power spectrum evaluated with different approximations to the one measured from simulations: in green is the Zel’dovich approximation, the red line is the T1 triangle with $k_1 = k_2$, $\theta = 90^\circ$. In blue we also plot the result obtained when adopting the approximation proposed in Winther et al. (2017). The MG model adopted is Hu–Sawicki $f(R)$ with $n = 1$ and $f_{R0} = -10^{-4}$. The dashed and dotted black lines mark, respectively, 5 per cent and 10 per cent deviation.

approximation (green lines) and for 2LPT approximated with the T1 triangle configuration (red lines), as well as the approximation proposed by Winther et al. (2017) (blue lines). The same quantities are computed for a Λ CDM simulation and plotted in Fig. 6 at redshift $z = 0$ (top panel) and $z = 1$ (bottom panel); here, the green line is again the Zel’dovich approximation, while the red line is 2LPT.

Since the fifth force introduced by the gravity modification enhances the clustering of matter, the value of σ_8 at $z = 0$ is larger for the $f(R)$ simulation than the Λ CDM one. In a sense, at a given redshift a universe with MG is *more non-linear* with respect to one where gravity is described by GR. Given that the perturbative approach breaks down as the field becomes non-linear, a fair comparison between MG and Λ CDM should be performed between snapshots with the same level of non-linearity. To assess the performance of our method with $f(R)$ gravity with respect to Λ CDM, we choose then two snapshots with the same value of σ_8 , and compare the halo power spectrum obtained for Λ CDM at redshift $z = 0$ (top panel of Fig. 6) to the $f(R)$ one at $z = 0.2$ (middle panel of Fig. 5).

In both cases, the second-order approximation allows to reproduce the halo power spectrum within 10 per cent up to

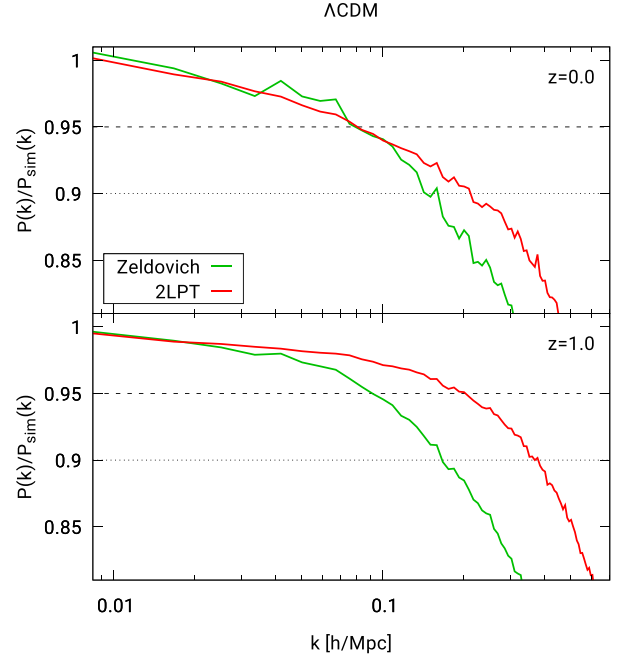


Figure 6. Ratio of the halo power spectrum for Λ CDM at $z = 0$ (top panel) and $z = 1$ (bottom panel) with respect to the simulation. The particles are displaced with the Zel’dovich approximation (first-order LPT, green line) or second-order LPT (red line). The dashed and dotted black lines mark, respectively, 5 per cent and 10 per cent deviation.

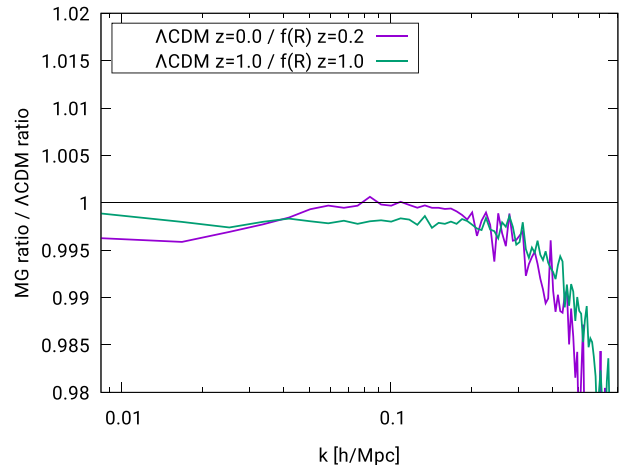


Figure 7. Ratio of the orange lines of Fig. 5 to the blue lines of Fig. 6 for $z = 1$ (green line) and $z = 0.2$ for MG versus $z = 0$ for Λ CDM (purple line).

$k \simeq 0.4 h \text{ Mpc}^{-1}$ at $z = 1$ and $k \simeq 0.2 h \text{ Mpc}^{-1}$ at $z = 0.2$ for $f(R)$. This result is very close to the one obtained for 2LPT with Λ CDM; to better quantify the performance of 2LPT with MG, we plot in Fig. 7 the ratio $(P_{\text{MG}}(k)/P_{\text{sim, MG}}(k))/(P_{\Lambda\text{CDM}}(k)/P_{\text{sim, } \Lambda\text{CDM}})$: the deviation between the two is within 1 per cent up to scales $k \simeq 0.4 h \text{ Mpc}^{-1}$. Moreover, we can see from Fig. 5 that the two approximations we considered (T1 and the one proposed in Winther et al. 2017) yield very similar results in terms of the halo power spectrum, even though they showed a few percent difference with respect to the full source term.

For the sake of completeness, we also compare the matter power spectrum obtained from our LPT-displaced particles to the one measured from the simulation. The results are shown in Fig. 8 for

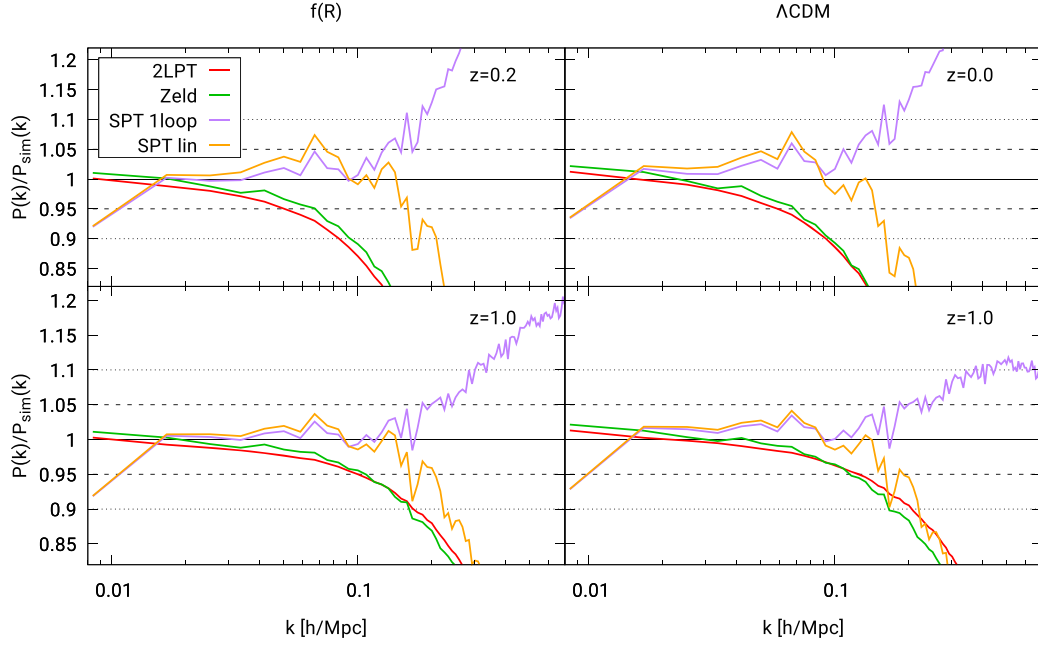


Figure 8. *Left column:* ratio of the matter power spectrum for the Hu–Sawicki $f_{R0} = -10^{-4}$ model, for $z = 0.2$ (top panel) and $z = 1$ (bottom panel). *Right column:* same quantity computed for Λ CDM, in this case the top panel refers to $z = 0$. The matter power spectrum is computed for different perturbative schemes: the Zel’dovich approximation (red line), 2LPT with particles displaced with the approximation proposed in this work (green line), linear Eulerian PT (orange line), and 1-loop Eulerian PT (violet line). The dashed and dotted black lines mark, respectively, 5 per cent and 10 per cent deviation.

Hu–Sawicki $f_{R0} = 10^{-4}$ (left column) and Λ CDM (right column), where we plot the ratio P/P_{sim} for the Zel’dovich approximation and 2LPT (green and red lines respectively), for $z = 0.2$ (top row, $z = 0$ in the Λ CDM case) and $z = 1$ (bottom row). In the same plot, we include the comparison with the results obtained for standard (Eulerian) perturbation theory, both linear (orange lines) and up to 1-loop (violet lines). The latter are computed with the MGPT code⁵ (Aviles & Cervantes-Cota 2017; Aviles et al. 2018). The performance of LPT in the case of matter is worse than in the case of haloes, with the power spectrum showing a significant loss of power on mildly non-linear scales. This behaviour is not unexpected: as shown in Munari et al. (2017a), the matter power spectrum computed with higher order LPT does not offer a significant improvement over the linear Zel’dovich approximation, in particular for realizations with interparticle distance \sim Mpc or below, and when the matter field is highly non-linear. The reason behind this is that displacing particles with higher order LPT produces more diffused structures, with an associated loss of power in the matter $P(k)$ already at intermediate scales. Such effect is not related to the presence of MG, but is only due to the perturbative approach to displacements, as can be seen by comparing the left and right columns of Fig. 8. On the other hand, the theoretical prediction computed with Eulerian PT is a better match to the N -body matter power spectrum, though the comparison with simulations is affected by sample variance.

Additionally, we perform a test to check the accuracy with which we reproduce the halo centres from particles displaced with our approximation, with respect to the simulation catalogues. The result is shown in Fig. 9 and Fig. 10, both for the first-order Zel’dovich approximation (green lines) and 2LPT (red and blue lines, same colour-coding as in Fig. 5, with the case of Λ CDM 2LPT plotted

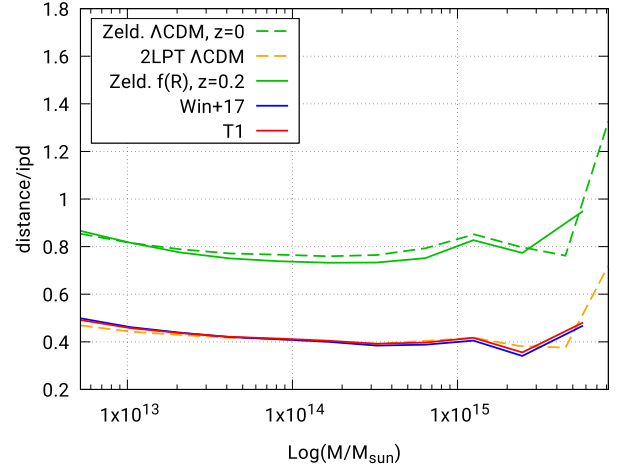


Figure 9. Distance between the halo centre as measured in the simulations to the one measured after halo reconstruction with the method described in Section 4 as a function of the halo mass, in units of interparticle distance (ipd , $0.977 \text{ Mpc } h^{-1}$). The dashed lines represent the median of the halo distance for the Λ CDM simulation at $z = 0$, while the solid lines represent the same quantity for the $f(R)$ simulation at redshift $z = 0.2$. The green lines refer to particles displaced with first-order LPT (Zel’dovich approximation), while the orange, blue, and red lines represent, respectively, the Λ CDM 2LPT, the approximation used in Winther et al. (2017) for $f(R)$ 2LPT, and the triangle configuration labelled as T1 in the previous plots.

in orange). Here, we plot the distance between the halo centres of the simulation and the ones in our catalogue, normalized to the interparticle distance (corresponding to $\sim 0.78 \text{ Mpc } h^{-1}$), as a function of the halo mass. To assess the performance of our 2LPT+MG approach, we compute halo distances also for the Λ CDM scenario (dashed lines in Fig. 9 and 10). As before, in order to do a fair comparison between the perturbative approaches in the

⁵<https://github.com/cosmoinin/MGPT>

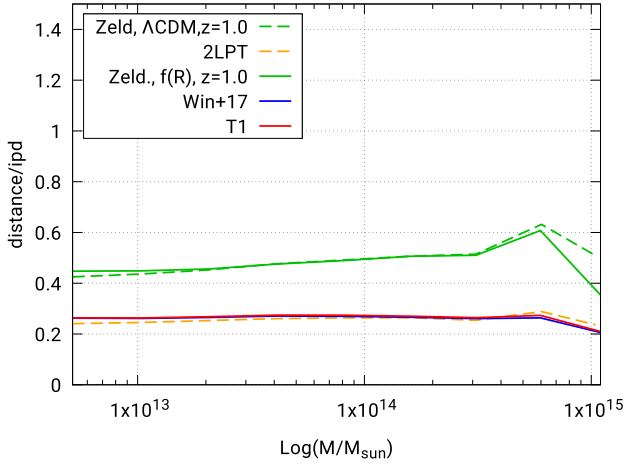


Figure 10. Same as Fig. 9 but at redshift $z = 1$.

two gravity models with the same level of non-linearity, we compare the Λ CDM one at $z = 0$ to the MG one at $z = 0.2$ (Fig. 9). It can be seen that even though there is on average an error of ~ 0.8 times the interparticle distance (green lines) for the first order, and ~ 0.4 times the interparticle distance for the second order, the performance is the same as the one shown by 2LPT+ Λ CDM. Moreover, the error on the halo position is roughly independent from the halo mass. In Fig. 10, we perform the same test but at redshift $z = 1$; as expected, the LPT halo centres are a better match to the simulation ones', and the performance for the MG model is again similar to the one obtained for the standard scenario.

5 TESTING A FIT FOR D_2

We test here if the technique used in Rizzo et al. (2017) for neutrinos gives acceptable results also in the case of $f(R)$ gravity. Massive neutrinos' free streaming imprints a scale-dependence to the growth of structures. The approach adopted in Rizzo et al. (2017) to extend the PINOCCHIO code to massive neutrino cosmologies is based on computing $D_1^2(k, a)$ as the ratio of the linear power spectrum evaluated at a generic a , over the same quantity calculated at a fixed time \bar{a} , where the latter is taken as the scale factor ensuring $D_1(k, \bar{a}) = 1$. Linear power spectra are computed with the CAMB code (Lewis & Bridle 2002). The second-order growth factor $D_2(t, k)$ is then computed by adopting the well-known fit, shown to be valid for a Λ CDM universe with standard GR (Bouchet et al. 1995):

$$D_2(k, a) = -\frac{3}{7} D_1^2(k, a) \Omega_m(a)^{-1/143}. \quad (33)$$

We adopt the same approach, to assess if it can be employed in the case of $f(R)$ gravity. To this purpose, we used EFTCAMB (Hu et al. 2015) to produce linear power spectra (computed for the same Hu–Sawicki $f(R)$ model discussed before) for a set of redshifts, and then input these power spectra to the code to compute the linear and second-order growth rate as described above.

In Fig. 11, we compare the second-order growth rate obtained from equation (33) to the one obtained by solving the second-order differential equation for the triangle T1 ($k_1 = k_2$, $\theta = 90^\circ$). In the top panel of Fig. 11, we plot the ratio between $D_2(k, a)$ and $-3D_1^2(k, a)/7$ as a function of $\Omega_m(a)$. The black line represents the best fit obtained by Bouchet et al. (1995) for a Λ CDM universe ($\Omega_m(a)^{-1/143}$), while the red, blue, orange, and green lines show

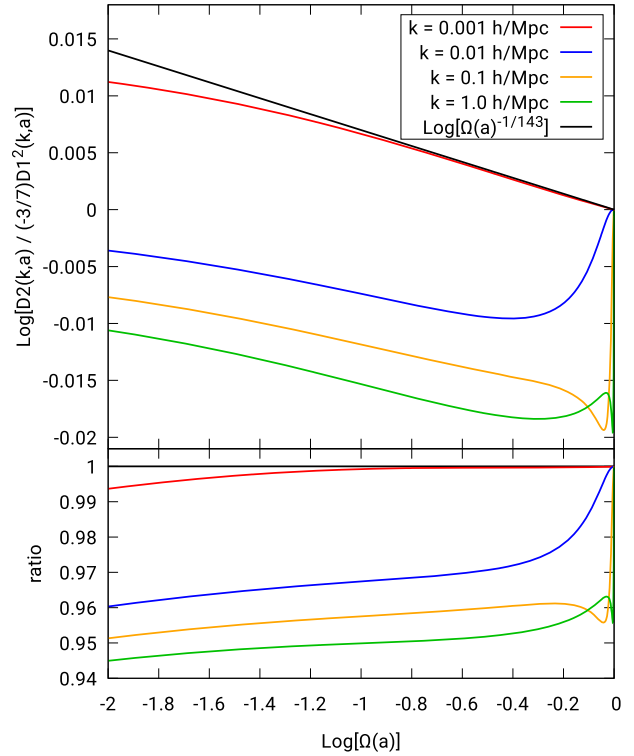


Figure 11. *Top panel:* Ratio of the second-order scale-dependent growth factor $D_2(k, a)$ to $(-3/7)D_1^2(k, a)$, as a function of $\Omega_m(a)$. The black line is the fit of Bouchet et al. (1995), $\Omega_m(a)^{-1/143}$, while the red, blue, orange, and green lines show $D_2(k, a)$ for different values of k , respectively, 0.001, 0.01, 0.1, and 1 h/Mpc . The MG model chosen is $n = 1$ Hu–Sawicki with $f_{R0} = -10^{-4}$. *Bottom panel:* Ratio of $D_2(k, a)/(-3/7)D_1^2(k, a)$ to $\Omega_m(a)^{-1/143}$. For small values of k (red line) the fit of Bouchet et al. (1995) is still valid, as expected, however, already for $k = 0.01 h/\text{Mpc}$, there is a deviation of $\sim 3-4$ per cent.

the ratio $D_2/(-3D_1^2/7)$ in the case of Hu–Sawicki $f(R)$ with $f_{R0} = -10^{-4}$, for increasing value of the wavenumber k as specified in the legend. The bottom panel shows the ratio of the lines of the top panel to $\Omega_m(a)^{-1/143}$. It can be seen that, in the case of scale-dependent growth induced by MG, equation (33) does not provide a good description for D_2 . In particular, even though the approximation is still accurate for the largest scales ($10^{-3} h \text{Mpc}^{-1}$, red line), where we do not expect significant effects of MG on the growth rates, for smaller scales (and already at $k = 10^{-2} h \text{Mpc}^{-1}$, blue line), the growth rate deviates for more than $\sim 3-4$ per cent from the fit, and the deviation gets stronger as we go to smaller scales. This is due to the fact that the scale dependence of $D_2(k, a)$ is not accurately modelled by $D_1^2(k, a)$. To properly treat mildly non-linear scales, we cannot use the fit of equation (33), and must therefore resort to the method described in the previous sections. The result of using this approximation to compute D_2 is shown in Fig. 12: here, we plot again the ratio of the halo power spectrum obtained with 2LPT to the N -body simulation one, and compare it to the one computed with the T1 triangle configuration. It is clear that the results obtained with the T1 triangle (red lines) are a better match to the simulation's halo $P(k)$ than the one obtained when using equation (33) (purple line). In particular, when adopting equation (33) to compute second-order displacements at $z = 1$, the resulting halo power spectrum does not show any improvements with respect to the linear approximation for scales $0.04 h \text{Mpc}^{-1} \leq k \leq 0.1 h \text{Mpc}^{-1}$ (bottom panel of Fig. 12).

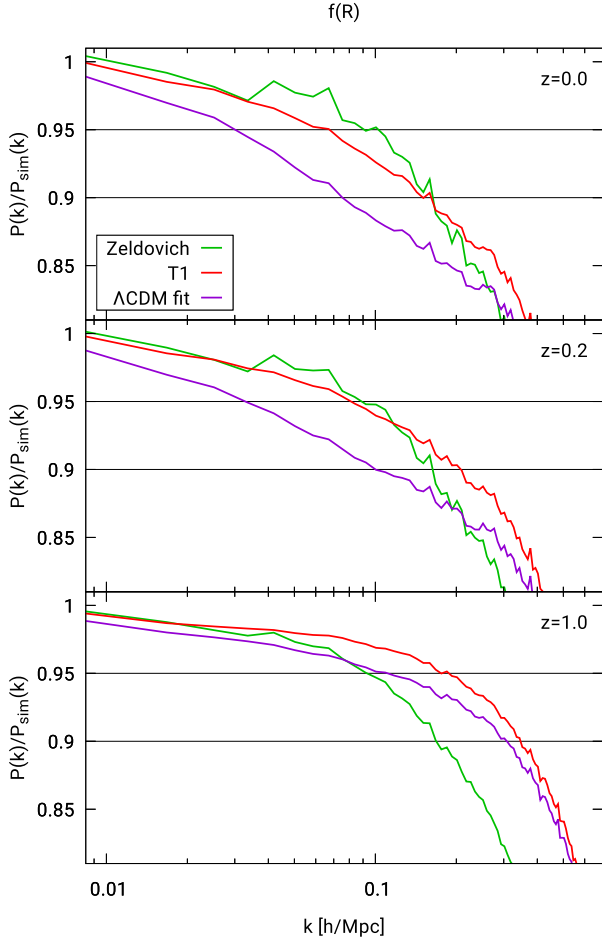


Figure 12. Comparison between the result obtained for the halo power spectrum when using the fit valid for Λ CDM (equation 33, shown in purple) to compute the second-order growth rate and the same quantity obtained when D_2 is computed by solving the differential equation for the T1 triangle configuration (red line). In green, we also show the result obtained for the first-order LPT, with $D_1(k, a)$ obtained by means of ratios of linear power spectra computed with EFTCAMB.

6 CONCLUSIONS

Future generations of galaxy redshift surveys will allow to measure the clustering of matter with a high degree of accuracy, allowing in principle to disentangle between different gravity theories. In order to test alternatives to GR, a proper treatment of non-linear and quasi-non-linear scales is required, since these are the scales where possible deviations from GR can be found. An adequate description of quasi-non-linear scales can be achieved via N -body simulations or, alternatively, with approximate methods. The latter allow, with some compromises on the accuracy, to generate the large sets of simulated catalogues needed to accurately constrain the cosmological parameters, a task that cannot be pursued with the computationally expensive N -body simulations. This work fits in the framework of extending these approximated methods to MG theories, focusing in particular on the computation of second-order Lagrangian displacements.

We presented a new computation of second-order LPT that is valid for a class of MG theories, and specialized it to the case of Hu–Sawicki $f(R)$ theory, testing its performances against N -body simulations. In MG theories, the various expansion terms of

LPT are typically not separable as products of time-dependent and space-dependent functions, and the equation for the second-order Fourier space Lagrangian potential $\phi^{(2)}(\mathbf{k}, a)$ can be written as an integral over two more vectors \mathbf{k}_1 and \mathbf{k}_2 , which are constrained to form a triangle with \mathbf{k} . For the case in which the coefficients M_k (equation 18) of the Taylor expansion of the fluctuations in the Ricci scalar δR are not scale-dependent, the differential equation for the 2LPT displacement potential can be written in terms of direct and inverse Fourier transforms. This allows to treat it with a numerical approach.

Using an initial density field sampled in cubic boxes of varying size and number of grid points, we numerically characterized the source term of the 2LPT potential (normalized by its GR counterpart) by computing its average and standard deviation as a function of k . We then considered different triangle configurations to find the second-order growth factor $D_2(k, k_1, k_2, a)$ that best reproduces the average of the source term, and used it to achieve an effective separation of the 2LPT displacement field into a space part, which does not depend on time and is equal to that used in GR, and a k -dependent second-order growth rate $D_2(k, a)$. The latter can be computed by numerically integrating a set of ordinary differential equations, one for each k value. The scatter in the numerical solution around the average source term gives a measure of the accuracy of this approximation, and is found to be moderate at the scales where 2LPT is relevant. We also tested the approximations we chose for $D_2(k, a)$ at different redshifts and for different values of the f_{R0} parameter, and found that the chosen triangle configurations can be safely adopted.

We implemented the solution for both differential equations for $D_2(k, a)$ in our code to compute Lagrangian displacements, and followed the approach discussed in Munari et al. (2017a) to test the accuracy level to which we can reproduce halo positions with respect to an N -body simulation. We produced a second-order displacement field, and compared with the results of a simulation run with MG–GADGET (Giocoli et al. 2018) and Hu–Sawicki $f(R)$ gravity (with a large value of $f_{R0} = -10^{-4}$, to maximize the effect of MG). The haloes in the simulation were identified by using a standard friends-of-friends halo finder algorithm. To construct our halo catalogue, we used the same particle assignment of the simulation to group particles displaced with 2LPT, then we re-computed each halo centre of mass as the average over all particles that belong to it. Using these halo displacements, we computed the halo power spectrum and compared it with that measured from the N -body halo catalogue. As demonstrated by Munari et al. (2017a) in the context of Λ CDM, this procedure allows to test how an approximate method like 2LPT can recover the clustering of haloes without being required to solve the much harder problem of identifying haloes themselves. We find that both chosen triangle configurations, together with the one previously proposed by Winther et al. (2017), perform well in terms of the halo power spectrum, allowing to reconstruct it within ~ 10 per cent at mildly non-linear scales ($k \simeq 0.2\text{--}0.4 h\text{Mpc}^{-1}$). This performance is the same (within 1 per cent) as the one shown by 2LPT in a standard, Λ CDM universe with GR, as highlighted in Fig. 7, meaning that the loss of power in our reconstructed halo $P(k)$ with respect to the N -body one is mostly due to the failure of the perturbative approach as the displacement field becomes non-linear. We conclude that LPT can be safely used to displace particles even in presence of MG.

The method we employ to construct the haloes, by matching the particle memberships to the simulation ones, means that we can perform an object-by-object analysis. We therefore verify how good our approximation for the halo displacements is at recovering the

halo positions with respect to the simulation. The result is again consistent with the one obtained in a Λ CDM scenario.

Throughout this work, we focused on a particular class of MG models, Hu–Sawicki $f(R)$. The method we propose is however quite general, and can be extended to other MG theories: once the functional form for the $\mu(k, a)$ function (that parametrizes the Fourier space Poisson equation) and the M_k coefficients are known, the procedure we propose can be employed to find a proper approximation for D_2 . If the M_k coefficients are scale-dependent the method can still be applied, provided that the S_3 (scalar field self-interaction) term of equation (31) can be written in terms of Fourier transforms. This requires identifying the proper operators in configuration space that correspond to the M_k coefficients in Fourier space. We stress that the procedure must be done only once for each gravity theory, and does not require the use of N -body simulations.

This allows to produce large sets of approximated simulations for different gravity models, a task that plays a crucial role in the computation of the covariance matrices needed to constrain cosmological parameters. We implemented MG scale-dependent growth in the PINOCCHIO code as an optional functionality, making it able to generate 2LPT displacements fields with MG. However, a key part of the algorithm is the one that groups particles in haloes, needed to make the code fully predictive. In the standard PINOCCHIO code, this is done by treating overdensities as homogeneous ellipsoids, and computing collapse times as the moment of first orbit crossing. This part of the algorithm still needs to be adapted to MG, so that the code can generate halo catalogues independently. This will involve formulating ellipsoidal collapse with MG, and is the focus of a future work.

ACKNOWLEDGEMENTS

The authors warmly acknowledge many discussions with the EFT-CAMB team, in particular with Alessandra Silvestri, Bin Hu, Marco Raveri, and Jorgos Papadomanolakis. This paper has benefited from the stimulating environment of the *Euclid* Consortium. CM and PM acknowledge support from the Italian Ministry for Education, University and Research (MIUR) grant PRIN 2015: *Cosmology and Fundamental Physics: illuminating the Dark Universe with Euclid* and from a *Fondo Ricerca di Ateneo* of the Trieste University. PM has been supported by the National Institute for Nuclear Physics (INFN) InDark research project. The DUSTGRAIN-pathfinder simulations employed in this work have been performed on the Marconi supercomputing machine at Cineca thanks to the Partnership for Advanced Computing in Europe (PRACE) project SIMCODE1 (grant nr. 2016153604) and on the computing facilities of the Computational Center for Particle and Astrophysics (C2PAP) and of the Leibniz Supercomputer Center (LRZ) under the project ID pr94ji.

REFERENCES

Abbott B. P. et al., 2016, *Phys. Rev. Lett.*, 116, 061102
 Amendola L. et al., 2018, *Living Rev. Relativ.*, 21, 2
 Avila S., Murray S. G., Knebe A., Power C., Robotham A. S. G., Garcia-Bellido J., 2015, *MNRAS*, 450, 1856

Aviles A., Cervantes-Cota J. L., 2017, *Phys. Rev. D*, 96, 123526
 Aviles A., Rodriguez-Meza M. A., De-Santiago J., Cervantes-Cota J. L., 2018, *J. Cosmol. Astropart. Phys.*, 2018, 013
 Baldi M., Villaescusa-Navarro F., Viel M., Puchwein E., Springel V., Moscardini L., 2014, *MNRAS*, 440, 75
 Blot L. et al., 2019, *MNRAS*, 485, 2806
 Bond J. R., Myers S. T., 1996, *ApJS*, 103, 1
 Bouchet F. R., 1996, in Bonometto S., Primack J. R., Provenzale A., eds, Proc. International School of Physics Course CXXXII, Dark Matter in the Universe. Oxford, IOS Press, p. 565
 Bouchet F. R., Colombi S., Hivon E., Juszkiewicz R., 1995, *A&A*, 296, 575
 Bull P. et al., 2016, *Phys. Dark Universe*, 12, 56
 Castorina E., Sefusatti E., Sheth R. K., Villaescusa-Navarro F., Viel M., 2014, *J. Cosmol. Astropart. Phys.*, 2014, 049
 Colavincenzo M. et al., 2019, *MNRAS*, 482, 4883
 De Felice A., Tsujikawa S., 2010, *Living Rev. Relativ.*, 13, 3
 Event Horizon Telescope Collaboration, 2019, *ApJ*, 875, L1
 Giocoli C., Baldi M., Moscardini L., 2018, *MNRAS*, 481, 2813
 Hu W., Sawicki I., 2007, *Phys. Rev. D*, 76, 064004
 Hu B., Raveri M., Silvestri A., Frusciantone N., 2015, *Phys. Rev. D*, 91, 063524
 Ishak M., 2019, *Living Rev. Relativ.*, 22, 1
 Izard A., Crocce M., Fosalba P., 2016, *MNRAS*, 459, 2327
 Joyce A., Jain B., Khoury J., Trodden M., 2015, *Phys. Rep.*, 568, 1
 Kitaura F.-S., Yepes G., Prada F., 2014, *MNRAS*, 439, L21
 Koda J., Blake C., Beutler F., Kazin E., Marin F., 2016, *MNRAS*, 459, 2118
 Koyama K., Taruya A., Hiramoto T., 2009, *Phys. Rev. D*, 79, 123512
 Laureijs R. et al., 2011, preprint ([arXiv:1110.3193](https://arxiv.org/abs/1110.3193))
 Levi M., et al., 2013, preprint ([arXiv:1308.0847](https://arxiv.org/abs/1308.0847))
 Lewis A., Bridle S., 2002, *Phys. Rev. D*, 66, 103511
 Lippich M. et al., 2019, *MNRAS*, 482, 1786
 LSST Science Collaboration, 2009, preprint ([arXiv:0912.0201](https://arxiv.org/abs/0912.0201))
 Martin J., 2012, *C. R. Phys.*, 13, 566
 Monaco P., 2016, *Galaxies*, 4, 53
 Monaco P., Theuns T., Taffoni G., 2002, *MNRAS*, 331, 587
 Munari E., Monaco P., Koda J., Kitaura F.-S., Sefusatti E., Borgani S., 2017a, *J. Cosmol. Astropart. Phys.*, 7, 050
 Munari E., Monaco P., Sefusatti E., Castorina E., Mohammad F. G., Anselmi S., Borgani S., 2017b, *MNRAS*, 465, 4658
 Perlmutter S. et al., 1999, *ApJ*, 517, 565
 Planck Collaboration, 2016, *A&A*, 594, A13
 Puchwein E., Baldi M., Springel V., 2013, *MNRAS*, 436, 348
 Riess A. G. et al., 1998, *AJ*, 116, 1009
 Rizzo L. A., Villaescusa-Navarro F., Monaco P., Munari E., Borgani S., Castorina E., Sefusatti E., 2017, *J. Cosmol. Astropart. Phys.*, 1, 008
 Sefusatti E., Crocce M., Scoccimarro R., Couchman H. M. P., 2016, *MNRAS*, 460, 3624
 Spergel D. et al., 2013, preprint ([arXiv:1305.5422](https://arxiv.org/abs/1305.5422))
 Stein G., Alvarez M. A., Bond J. R., 2019, *MNRAS*, 483, 2236
 Tassev S., Zaldarriaga M., Eisenstein D. J., 2013, *J. Cosmol. Astropart. Phys.*, 6, 036
 Valogiannis G., Bean R., 2017, *Phys. Rev. D*, 95, 103515
 Weinberg S., 1989, *Rev. Mod. Phys.*, 61, 1
 Winther H. A., Koyama K., Manera M., Wright B. S., Zhao G.-B., 2017, *J. Cosmol. Astropart. Phys.*, 8, 006
 Wright B. S., Koyama K., Winther H. A., Zhao G.-B., 2019, *J. Cosmol. Astropart. Phys.*, 6, 040
 Zel'dovich Y. B., 1970, *A&A*, 5, 84

This paper has been typeset from a $\text{\TeX}/\text{\LaTeX}$ file prepared by the author.